Available online at www.sciencedirect.com

ScienceDirect

Geochimica et Cosmochimica Acta 302 (2021) 1–17

Geochimica et Cosmochimica Acta

www.elsevier.com/locate/gca

Entropy, dynamics, and freezing of $CaSiO_3$ liquid

Alfred Wilson [a], Lars Stixrude [a,b,*]

[a] Department of Earth Sciences, University College London, London WC1E 6BT, UK
[b] Department of Earth, Planetary, and Space Sciences, University of California, Los Angeles, CA 90095-1567, USA

Received 14 April 2020; accepted in revised form 12 March 2021; available online 24 March 2021

Abstract

We present first principles predictions of the absolute entropy of a silicate liquid ($CaSiO_3$) over a wide pressure-temperature range encompassing the Earth's mantle (2000–6000 K, 0–270 GPa). The results are derived from molecular dynamics simulations based on density functional theory and the two-phase thermodynamic (2PT) method, which divides the vibrational density of states into solid-like and gas-like parts, and which we describe in detail. The heat capacity derived from the absolute entropy agrees well with experimental measurements at low pressure. We find that the vibrational contribution accounts for more than 75% of the total entropy over the range of our study. We find that the two-body approximation to the excess entropy (relative to the ideal gas), which is computed with knowledge only of the radial distribution function, is excellent over most of the range considered, except at the lowest pressures and temperatures. We also compute the entropy of $CaSiO_3$ perovskite and use the entropy of liquid and solid phases to determine their absolute free energies and the melting curve. The melting curve agrees well with experiment and independent theoretical determinations based on Clausius-Clapeyron integration and the ZW method, showing a melting temperature of 5600 K at the Earth's core-mantle boundary. We find a nearly universal scaling of the self-diffusion coefficients with the excess entropy $D^* = 0.9\exp(1.2S_{ex})$, where D^* is the self-diffusion coefficient suitably non-dimensionalized using macroscopic thermodynamic properties, and S_{ex} is the excess entropy in units of the Boltzmann constant per atom. We use our results to estimate the temperature distribution in an isentropic, molten silicate Earth, finding 4.4 kJ/kg/K to be the lowest entropy that is completely molten, and producing a temperature at the core-mantle boundary of 6000 K.

Keywords: Mantle; Silicate liquids; Thermodynamics; Equation of state; Ab initio theory

1. INTRODUCTION

Entropy is central to our understanding of the role of silicate melts in geologic processes. For example, the entropy and melting temperature determine the latent heat of melting, an energy source that can affect processes ranging from magma chamber crystallization (Huber et al., 2009) to magma transport (Blundy et al., 2006), to magma ocean evolution (Labrosse et al., 2007). The entropy of melting, along with the volume of melting, determines the slope of the melting curve in one-component systems, via the Clausius-Clapeyron equation, and thus the melting temperature at elevated pressure (Stixrude and Karki, 2005); in multi-component systems like the mantle, the slope of liquidus and solidus also depends on the partial molar entropies and volumes (Walker et al., 1988). In the early Earth, the entropy establishes a connection between the energetics of impacts and the subsequent thermal state of the mantle (Lock and Stewart, 2017). The entropy is central to the computation of the Gibbs free energy G and therefore phase equilibria

$$G(P,T) = H(P,T) - TS(P,T) \quad (1)$$

* Corresponding author at: Department of Earth, Planetary, and Space Sciences, University of California, Los Angeles, CA 90095-1567, USA.
E-mail address: lstixrude@epss.ucla.edu (L. Stixrude).

https://doi.org/10.1016/j.gca.2021.03.015
0016-7037/

where the enthalpy H at a given pressure P and temperature T is easily computed from molecular dynamics simulations, but the entropy is not.

Our knowledge of the entropy of silicate liquids is still very limited. This is in part due to the challenge of determining the entropy of liquids from experimental or computational methods. Experimentally it is not possible to measure the absolute value of the entropy. The best one can do is to measure changes in the entropy, for example, by measuring the heat capacity. By integrating the heat capacity and relating the entropy of the liquid to that of the solid via the heat of melting, the absolute value of the entropy of the liquid can then be calculated (Richet, 1984). A similar limitation applies to simulations: whereas most thermodynamic properties, such as pressure or internal energy, can be expressed as time-averages over a phase-space trajectory, the entropy cannot, as it depends on the volume of phase space accessible to the system, as measured formally by the partition function Q, via $S = k \ln Q$ (Haile, 1992).

The entropy of liquids is poorly understood theoretically. The reason is that the structure and dynamics of liquids differ fundamentally from those of the much better understood limits of solids or gases. In the case of gases, the problem is simplified by weak interactions between the constituent atoms. In the limit of no interactions, the entropy of the ideal gas is given analytically by the famous Sackur-Tetrode equation (McQuarrie, 1976). In the case of solids, configuration space may be enumerated by the normal modes of vibration of the lattice (phonons), and the entropy expressed as a sum over the occupations of these vibrational states (Born and Huang, 1954). Liquids are more challenging, because, unlike the gas, interatomic interactions are important, and, unlike the solid, atomic motions are not only vibrational in character, but also diffusional, with no equivalent of the harmonic restoring force.

Here we present and apply a method for computing the entropy that has found success in application to simple liquids and molecular liquids, but which has not previously been applied to silicate liquids (Lai et al., 2012; Desjarlais, 2013). We focus on the $CaSiO_3$ system because the thermochemical properties of the liquid and glass are well known at 1 bar (Richet and Fiquet, 1991), and the melting curve has been studied over a wide pressure range encompassing the perovskite stability field (Zerr et al., 1997). Moreover, the perovskite-phase melting curve has been studied theoretically via two distinct first principles approaches, leading to consistent results (Braithwaite and Stixrude, 2019). Previous experimental and theoretical results on $CaSiO_3$ form an ideal basis against which to compare our predictions.

The two-phase thermodynamic (2PT) method, explicitly recognizes the unique features of the liquid by dividing its entropy into solid-like and gas-like contributions. The division is made in the context of the vibrational density of states, which, unlike a solid, maintains a finite value at zero frequency, corresponding to diffusional modes. We first review approaches to understanding the contributions to the entropy of silicate liquids as they have been discussed in the literature, such as configurational entropy and excess entropy. We then present the 2PT method, introducing the underlying statistical mechanical concepts such as the velocity auto-correlation function, and the vibrational density of states. We then discuss the computational implementation of the 2PT method in our molecular-dynamics simulations. We then apply the method to $CaSiO_3$ liquid and test our results for internal consistency, and against experimental measurements and independent computational determinations of the melting curve of $CaSiO_3$ perovskite. The results lead to additional insight into the contributions to the entropy of silicate liquids over a wide range of pressure and temperature, and also to the dynamics of silicate liquids, which we then explore.

2. ENTROPY

Comparison to the gas and the solid motivate two different ways of thinking about the contributions to the entropy of the liquid. Because the entropy of the ideal gas S_{IG} is well known, one defines the excess entropy S_{ex} as

$$S(V,T) = S_{IG}(V,T) + S_{ex}(V,T) + S_{el}(V,T) \tag{2}$$

where S is the total entropy, S_{el} is the electronic entropy, and S_{ex} is a negative quantity, i.e. the entropy of the liquid is always less than that of the ideal gas at the same volume and temperature because atomic positions are correlated (Stebbins et al., 1984). The entropy of the ideal gas is (McQuarrie, 1976)

$$\frac{S_{IG}}{k} = \frac{5}{2} + \sum\nolimits_{\alpha}\left[x_\alpha \ln\left(\frac{V}{N\Lambda_\alpha}\right) - x_\alpha \ln x_\alpha\right] \tag{3}$$

where the de Broglie thermal wavelength $\Lambda_\alpha = h/\sqrt{2\pi m_\alpha kT}$, m_α is the atomic mass, h is the Planck constant, k is the Boltzmann constant, and the sum is over atom types α. The electronic entropy is usually ignored in the context of silicate liquids, but we have found it to be non-negligible at mantle conditions (de Koker et al., 2013; Stixrude et al., 2020). It is formally possible to write the excess entropy as a sum over the contributions from n-body correlations. As the terms rapidly become cumbersome with increasing n, truncation at the lowest order ($n = 2$) has been widely studied, leading to (Baranyai and Evans, 1989; Sharma et al., 2008; Goel et al., 2011)

$$S_{ex} \approx s_2 = -\frac{Nk}{2V}\sum\nolimits_{i=1}^{N}\sum\nolimits_{j=1}^{N} x_i x_j \int_0^\infty \left\{g_{ij}(r)\ln g_{ij}(r) - \left[g_{ij}(r) - 1\right]\right\} 4\pi r^2 dr \tag{4}$$

where N is the total number of atoms, V is the volume, x_i is the mole fraction of atom i, and $g_{ij}(r)$ is the partial radial distribution function. The two-body approximation has the further advantage of being experimentally measurable via the Fourier-transform of the structure factor (Goel et al., 2011). To understand the expression for s_2, consider the limit of the ideal gas, for which $g_{ij}(r) = 1$ for all r. Then the integrand vanishes as does s_2 and the excess entropy. One manifestation of the structure of a liquid is an excluded volume at small r caused by the repulsion between atoms. Over this excluded volume, $g_{ij}(r) = 0$, and the integral is just $4\pi r_{excl}^3/3$, where r_{excl} is the radius of the excluded volume, leading to a finite (negative) contribution to s_2 and the excess

entropy. Correlations in the liquid are important at larger distances as well: $g_{ij}(r)$ approaches unity only at many times the interatomic spacing for densities and temperatures typical of silicate liquids in the mantle, so accurate radial distribution functions and a quantitative evaluation of the integral is essential. The accuracy of the 2-body approximation to the excess entropy has not previously been evaluated in the context of silicate liquids. Studies of simple liquids for which the exact entropy is known have shown that the n-body expansion may converge slowly and that higher order correlations can be important (s_3 etc.), particularly at high density (Baranyai and Evans, 1991).

Alternatively, we may use the glass as a reference for understanding the entropy of the liquid

$$S(V,T) = S_{vib}(V,T) + S_{conf}(V,T) + S_{el}(V,T) \tag{5}$$

where the first term arises from vibrational modes and the second is the remainder (aside from the electronic contribution) and is referred to as configurational. In a pure, defect-free crystalline solid, the entropy is entirely vibrational and the configurational entropy is zero. In the liquid, the configurational entropy is non-zero and increases with increasing temperature as manifested in the configurational heat capacity

$$C_{V,\ conf} = T\left(\frac{\partial S_{conf}}{\partial T}\right)_V \tag{6}$$

which is uniformly positive for silicate liquids (Mysen and Richet, 2018). The entropy of glasses, like crystals, is dominated by vibrational entropy, which is usually slightly larger than that of the crystal at the same pressure and temperature (Richet et al., 1991). Glasses also show a non-zero configurational entropy, which is independent of temperature and persists even at zero temperature (Richet, 1984). This so-called residual entropy is due to the disorder in the glass that is frozen in when the liquid passes through the glass transition temperature on cooling. A number of studies have linked the configurational entropy of silicate liquids and glasses to populations of structural units such as coordination environments or anion speciation (Lee and Stebbins, 2002; Lee et al., 2020).

The excess entropy and the configurational entropy play an important role in theories of the dynamics of liquids. For example, the viscosity is related to the configurational entropy in several theoretical approaches (Mauro et al., 2009), including that of Adam and Gibbs (Adam and Gibbs, 1965). Other authors have argued that transport properties, including the viscosity and the self-diffusion coefficient, are better related to the excess entropy (Rosenfeld, 1999).

A note on units. We express the entropy and the heat capacity in units of k/atom as in many previous studies (Alfè, 2005; de Koker and Stixrude, 2009; Desjarlais, 2013). In these units the heat capacity of many condensed phases at high temperature is near 3 (the Dulong-Petit limit of solids) and the entropy of melting of many systems is close to unity. We can then compare directly with the near universal result for the entropy of melting of simple liquids at high pressure that has appeared in the literature: $k$ln2/atom (Stishov et al., 1973). The units k/atom are identical to the units R/mol/atom, or as these units are sometimes referred to in the literature: R per g·atom (Stebbins et al., 1984), where R is the gas constant $R = kN_A$, and N_A is the Avogadro number. An example facilitates comparison with other units used in the literature: the entropy of liquid $CaSiO_3$ at the 1 bar melting point (1821 K) reported by (Richet et al., 1991) as 324.86 J/mol/K is equal to 7.8145 k/atom and 2.7966 kJ/kg/K. For consistency we also report other extensive quantities as per mol per atom (per mol of atoms), including the volume and the internal energy.

3. THEORY

3.1. Background

The 2PT method relies on basic concepts from statistical mechanics including the velocity auto-correlation function, its Fourier transform, its spectral decomposition into moments, and the memory function. Before describing the 2PT method, we discuss these basic ingredients, making connections to experimental observables, to show examples from our simulations, and discuss computational practicalities.

3.2. Velocity auto-correlation function

One way to see the relationship between the behavior of gases, liquids, and solids, is through the velocity auto-correlation function (McQuarrie, 1976)

$$\Phi_\alpha(t) = \frac{\left\langle \vec{v}_\alpha(t) \cdot \vec{v}_\alpha(0) \right\rangle}{\left\langle \vec{v}_\alpha(0) \cdot \vec{v}_\alpha(0) \right\rangle} \tag{7}$$

where the subscript α refers to one atom type, t is time, $\vec{v}_\alpha(t)$ is the velocity at time t, and the angle brackets indicate an average over all atoms of type α, and all time origins. The denominator is just the mean-squared velocity

$$\left\langle \vec{v}_\alpha(0) \cdot \vec{v}_\alpha(0) \right\rangle = \frac{3kT}{m_\alpha} \tag{8}$$

The normalization sets $\Phi_\alpha(t) = 1$ at $t = 0$.

The velocity auto-correlation function specifies the degree to which velocities at time zero are correlated with those at some later time t. In an ideal gas, perfect correlation is maintained at all times because atom–atom interactions are neglected: atoms never collide and therefore never change their velocity and the velocity autocorrelation function remains unity for all times. In a perfectly harmonic solid the velocity auto-correlation function is harmonic, and oscillates about zero: atoms initially moving in one direction slow and reverse, so that Φ diminishes rapidly with time and is -1 at half a vibrational period.

The velocity auto-correlation function of the liquid lies in between these two extremes (Fig. 1). Strong interactions cause Φ to decay towards zero rapidly. Oscillations about zero appear, but are rapidly damped because of anharmonicity and diffusion.

3.3. Vibrational density of states and diffusion

The liquid is most clearly distinguished from the solid by the vibrational density of states, which is the cosine trans-

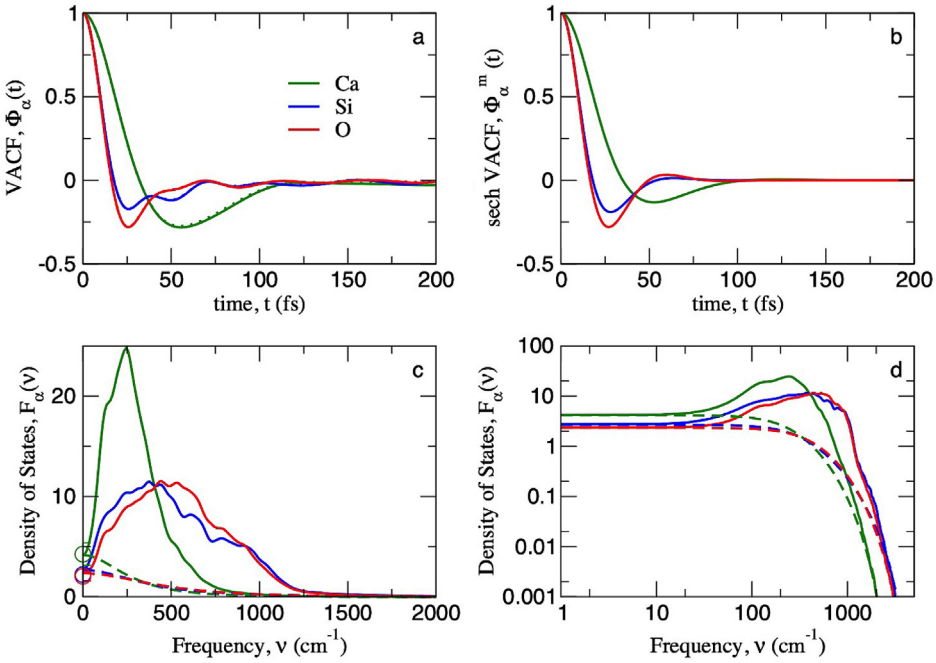

Fig. 1. (a) The velocity auto-correlation function of $CaSiO_3$ liquid at 4000 K and 5.66 cm^3 mol^{-1} atom^{-1} (P = 47 GPa). The solid lines are undamped, the nearly coincident dashed lines are with damping applied. (b) The model velocity auto-correlation function of (Isbister and McQuarrie, 1972) (Eq. (15)) computed from the second and fourth moments of the vibrational density of states. (c) The vibrational density of states computed as the cosine transform of the velocity auto-correlation function (solid: total vibrational density of states, $F_\alpha(\nu)$, dashed: the gas fraction $f_\alpha F_\alpha^g(\nu)$. The $F_\alpha$are reported in units of PHz^{-1} or fs. The circles are values of the normalized self-diffusion coefficient $D_\alpha m_\alpha/kT$ with $D_\alpha$computed independently from the mean-squared displacement as we have done in our previous studies (de Koker et al., 2008). (d) The vibrational density of states in log–log space to show the convergence of the gas-fraction with the total at large frequencies.

form of the velocity auto-correlation function (Dickey and Paskin, 1969; Berens et al., 1983)

$$F_\alpha(\nu) = \int_0^\infty \Phi_\alpha(t)\cos(2\pi\nu t)dt \tag{9}$$

the normalization is such that

$$\int_0^\infty 12F_\alpha(\nu)d\nu = 3 \tag{10}$$

and ν is the frequency.

In the liquid, the vibrational density of states is finite at zero frequency, whereas F vanishes at zero frequency in the solid. The zero frequency modes correspond to diffusional motion (i.e. no restoring force): the self-diffusion coefficient is given by the vibrational density of states at zero frequency

$$D_\alpha = \frac{kT}{m_\alpha}F_\alpha(0) = \frac{kT}{m_\alpha}\int_0^\infty \Phi_\alpha(t)dt \tag{11}$$

It will prove convenient to introduce a dimensionless parameter related to the self-diffusion coefficient

$$\Delta_\alpha = \frac{8}{3}F_\alpha(0)\sqrt{\frac{\pi kT}{m_\alpha}}\bar{V}_\alpha^{-1/3}\left(\frac{6}{\pi}\right)^{2/3} \tag{12}$$

where $\bar{V}_\alpha$ is the partial molar volume of atom type α (Lai et al., 2012).

The vibrational density of states of the liquid (Fig. 1) shows peaks corresponding to vibrational modes. The finite width of these peaks is due to anharmonicity, i.e. the finite lifetime of vibrational modes due to phonon–phonon interactions, as well as structural disorder. In the liquid the vibrational modes are very short-lived, as they are interrupted by diffusional hops, and the peaks are very broad. The heavier atom (Ca) shows mean vibrational frequencies that are less than that of the lighter atoms (Si and O). The vibrational density of states has a finite value at zero frequency, reflecting the self-diffusion coefficient (Eq. (11)).

To further illustrate the vibrational density of states and make contact with experiment, we compare the vibrational density of states of the liquid to experimental observations of $CaSiO_3$ glass at ambient pressure (Fig. 2). This comparison is illustrative rather than quantitative because in the experiment, the vibrational density of states is convolved with the selection rules of the probe (Raman or IR). Nevertheless, many similarities are apparent including the range of frequencies observed, and the value of the highest frequencies. Although the liquid simulation is at 2000 K and 4.4 GPa, and the experimental data are at 300 K and 1 bar, the volumes of the liquid and glass are very similar in this comparison. We show below that the mean properties of the vibrational density of states are most strongly dependent on volume, rather than on temperature or pressure.

3.4. Moments

The velocity auto-correlation function can be written exactly as an infinite MacLaurin series in time with coefficients given by the even moments of the vibrational density of states (Douglass, 1961)

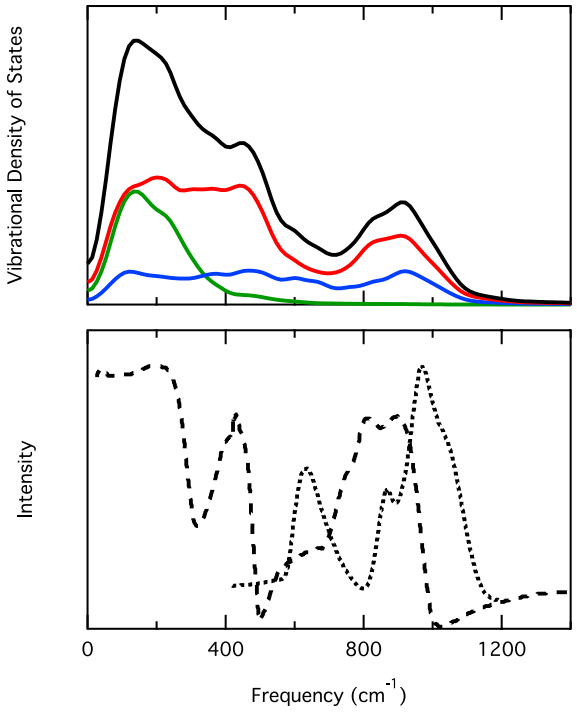

Fig. 2. (top) Vibrational density of states at 7.90 cm^3 mol^{-1} $atom^{-1}$ and 2000 K (4.4 GPa) showing the total (black) and the contributions from each atom type $x_\alpha F_\alpha(v)$, where x_α is the atomic fraction: Ca (green), Si (blue), O (red) compared with (bottom) the experimentally measured Raman (short dashed) (Retsinas et al., 2016) and IR reflectance (long dashed) (Meneses et al., 2006) spectra of $CaSiO_3$ glass at ambient conditions ($V = 8.025$ cm^3 mol^{-1} $atom^{-1}$). (For interpretation of the references to colour in this figure legend, the reader is referred to the web version of this article.)

$$\Phi_\alpha(t) = \sum_{n=0}^{\infty}(-1)^n \frac{M_{2n}}{(2n)!} t^{2n} \tag{13}$$

where the moments are defined

$$M_k = \langle v^k \rangle = \frac{\int_0^\infty v^k F(v) dv}{\int_0^\infty F(v) dv} \tag{14}$$

The analysis of the moments of the vibrational density of states is well developed in the case of solids (Barron et al., 1957). It has been shown that at high temperature thermodynamic properties become sensitive only to the low-order moments of the vibrational density of states, and do not depend on the details of the phonon spectrum. For example, the entropy of mantle crystalline phases is given to within a few percent by the zeroth moment of the vibrational density of states (Stixrude and Lithgow-Bertelloni, 2005).

To see how low-order moments can capture much of the dynamics in the liquid, we consider the model velocity auto-correlation function of (Isbister and McQuarrie, 1972). We do not make use of this model in our computations of entropy, but find it useful to understand the origin of features in the velocity auto-correlation function. The model velocity auto-correlation function has the simple functional form

$$\Phi_\alpha^m(t) = \mathrm{sech} a_\alpha t \cos b_\alpha t \tag{15}$$

with the values of the two coefficients chosen to match the two lowest-order moments (M_2 and M_4) as determined from our simulations. The relations are easily obtained by expanding Eq. (15) as a MacLaurin series and comparing terms with Eq. (13). The resulting approximate velocity auto-correlation function indeed captures many of the features of the full function, including the slower decay of the more massive atom (Ca), and the oscillations about zero (Fig. 1).

The low-order moments play an important role in the 2PT method to be described. We have found that computation of the moments from Eq. (14) is numerically unstable because it is sensitive to the high-frequency, low-amplitude portion of the vibrational density of states. A more stable route is the following exact relation (Isbister and McQuarrie, 1972)

$$M_{2n} = \frac{\left\langle \vec{v}^{(n)}(0) \cdot \vec{v}^{(n)}(0) \right\rangle}{\frac{3kT}{m}} \tag{16}$$

where $\vec{v}^{(n)}$ is the nth time-derivative of the velocity. The required time derivatives are readily computed via interpolation of the dynamical trajectories of the atoms in the simulation.

3.5. Memory function

To further explore the properties of the velocity auto-correlation function, we introduce the memory function K_α defined by

$$\frac{d\Phi_\alpha}{dt} = -\int_0^t K_\alpha(\tau)\Phi_\alpha(t-\tau)d\tau \tag{17}$$

The memory function is a useful starting point for approximation because it can be shown that it decays much more rapidly than the velocity auto-correlation function. For example, if the memory function takes the simplest possible functional form: a delta function

$$K_\alpha(\tau) = \xi_\alpha \delta(\tau) \tag{18}$$

the velocity auto-correlation function is

$$\Phi_\alpha(t) = e^{-\xi_\alpha t} \tag{19}$$

The density of states is given by the general expression

$$F_\alpha^g(v) = \frac{1}{2}\left[\frac{1}{\widehat{K}_g^\alpha(i2\pi v) + i2\pi v} + \frac{1}{\widehat{K}_g^\alpha(-i2\pi v) - i2\pi v}\right] \tag{20}$$

where $\widehat{K}_g^\alpha$ is the Laplace transform of the memory function, yielding, for the delta memory function

$$F_\alpha(v) = \frac{F_\alpha(0)}{1 + (2\pi v/\xi_\alpha)^2} \tag{21}$$

and the so-called friction coefficient

$$\xi_\alpha = \frac{kT}{m_\alpha D_\alpha} \tag{22}$$

This form of the memory function was assumed in initial applications of the 2PT method (Lin et al., 2003). It is incorrect in the sense that the time derivative of the memory function does not vanish at the origin as it is theoretically required to do (Berne et al., 1966). More importantly for

us, it turns out not to satisfy observed properties of the vibrational density of states of condensed systems: the Lorentzian form (Eq. (21)) decays too slowly with increasing frequency at large frequency (Desjarlais, 2013). Below we introduce a generalization, a Gaussian form of the memory function, which overcomes these difficulties.

3.6. The two-phase thermodynamic (2PT) method

We have now assembled all of the pieces that we need to present the 2PT method. The development follows the original formulation by (Lin et al., 2003), its generalization to multi-component fluids (Lai et al., 2012), and the modification of the memory function advanced by (Desjarlais, 2013).

The presence of diffusional and vibrational modes in the liquid motivates a division of the vibrational density of states into a gas-like part F^g_α, and a solid-like partF^s_α

$$F_\alpha(v) = f_\alpha F^g_\alpha(v) + (1-f_\alpha)F^s_\alpha(v) \tag{23}$$

where f_α is the gas-like fraction, which is to be determined. The entropy of the liquid is

$$S(V,T) = S_{el}(V,T) + k\sum_\alpha \left\{ x_\alpha \int_0^\infty dv \left[f_\alpha F^g_\alpha(v) W^g_\alpha + (1-f_\alpha)F^s_\alpha(v)W^s(v)\right] - x_\alpha \ln x_\alpha \right\} \tag{24}$$

where we have defined gas-like and a solid-like kernels, $W^g_\alpha$and W^s and the last term arises from mixing of the components (Lai et al., 2012). The first term is the electronic entropy.

The kernel for the solid-like part is the Bose-Einstein expression for a collection of harmonic oscillators (Born and Huang, 1954)

$$W^s(v) = 3\left\{ \frac{hv/kT}{\exp(hv/kT)-1} - \ln\left[1-\exp(-hv/kT)\right] \right\} \tag{25}$$

which is independent of atom type. The harmonic theory is not a serious restriction. Wallace (Wallace, 1972) has shown that the entropy of an anharmonic solid is accurately captured by the harmonic kernel; the effect of anharmonicity is to modify (re-normalize) the vibrational density of states (Fultz, 2010), an effect that is captured by our molecular dynamics simulations.

The gas-like kernel is given by the entropy of the hard-sphere fluid (Carnahan and Starling, 1970)

$$W^g_\alpha = \frac{S_{IG\alpha}}{k_B} + \ln\left[\frac{1+\gamma_\alpha+\gamma_\alpha^2-\gamma_\alpha^3}{(1-\gamma_\alpha)^3}\right] + \frac{3\gamma_\alpha^2-4\gamma_a}{(1-\gamma_\alpha)^2} \tag{26}$$

which is independent of frequency, where γ_α is the hard-sphere packing fraction. The ideal gas contribution is

$$\frac{S_{IG\alpha}}{k} = \frac{5}{2} + \ln\left(\frac{\bar{V}_\alpha}{\Lambda^3_\alpha f_\alpha}\right) \tag{27}$$

The hard-sphere packing fractions are determined by relating the self-diffusion coefficient to the Enskog result for hard-spheres (Alder et al., 1970), leading to (Lin et al., 2003; Desjarlais, 2013)

$$\frac{2(1-\gamma_\alpha)^3}{2-\gamma_\alpha} = \gamma_\alpha^{2/5}\Delta_\alpha^{3/5} \tag{28}$$

which is solved numerically for the γ_α.

To proceed, we need to specify a form of the gas-like vibrational density of states. Instead of a delta memory function, (Desjarlais, 2013) proposed a Gaussian form

$$K^g_\alpha(\tau) = A_\alpha \exp(-B_\alpha \tau^2) \tag{29}$$

with Laplace transform

$$\widehat{K}^g_\alpha(s) = K_{0\alpha} w(-\eta) \tag{30}$$

where $K_{0\alpha} = A_\alpha\sqrt{\pi/4B_\alpha}$, $\eta = s/2\sqrt{B_\alpha}$, and w is the Faddeeva function

$$w(z) = e^{-z^2}\mathrm{erfc}(-iz) \tag{31}$$

where i is the imaginary unit. The following relations complete the definition of F^g_α by determining the values of f_α, A_α, and B_α (Desjarlais, 2013)

$$f_\alpha = \frac{F_\alpha(0)}{F^g_\alpha(0)} = \frac{A_\alpha F_\alpha(0)}{2}\sqrt{\frac{B_\alpha}{\pi}} \tag{32}$$

$$\frac{4B_\alpha}{A_\alpha} = 2 + \sqrt{\pi\left(1+\frac{4B_\alpha F^2_\alpha(0)}{\gamma_\alpha^{4/5}\Delta_\alpha^{6/5}}\right)} \tag{33}$$

$$B_\alpha = \frac{f_\alpha\left(2M_2A_\alpha - M_4 - A_\alpha^2\right) + M_4 - M_2^2}{2f_\alpha(1-f_\alpha)A_\alpha} \tag{34}$$

The first of these relations arises from the fact that the solid-like vibrational density of states vanishes at zero frequency. The second comes from requiring the low frequency portion of the density of states derived from Gaussian and delta (Eq. (21)) memory functions to agree. The final one guarantees that the first two even moments of the velocity auto-correlation function are matched.

Following (Desjarlais, 2013), we also make use of an alternative prescription in which B_α is determined not by Eq. (34) (*moments method*), but by requiring the gas-like density of states to merge smoothly with the total density of states at high frequency (*matching method*). We use the difference in the gas-like contribution to the entropy computed using these two different methods as a measure of the uncertainty in the entropy.

We compute the entropy of the solid phase from the same equations but with the gas fractions and the entropy of mixing set to zero. This leads to the standard expression for the entropy of a perfect crystal with purely vibrational entropy (Born and Huang, 1954; Wallace, 1972), which has been used in many previous molecular dynamics studies of the solid state (Fultz, 2010).

4. COMPUTATION

The setup of the first principles molecular dynamics simulations follows our previous work (Stixrude and Karki, 2005; de Koker et al., 2008; Sun et al., 2011; Scipioni et al., 2017) and is identical to the canonical ensemble simulations of (Braithwaite and Stixrude, 2019). Briefly, our simulations are based on density functional theory in the

PBEsol approximation to the exchange–correlation functional (Perdew et al., 2008) and the projector augmented wave (PAW) method (Kresse and Joubert, 1999) as implemented in VASP (Kresse and Furthmuller, 1996). We use PAW potentials with, respectively, for Ca, Si, and O: 10, 4, and 6 valence electrons and core radii of 1.22. 1.01, and 0.80 Å. We assume a basis set size given by an energy cutoff of 500 eV and Brillouin zone sampling at the Gamma point only, which leads to convergence of energy and pressure to within 7 meV per atom and 0.3 GPa, respectively (Fig. S1). We assume thermal equilibrium between ions and electrons via the Mermin functional (Mermin, 1965); indeed, we have found that thermal excitation of electronic states is non-negligible over the range of pressure and temperature in the Earth's mantle (de Koker and Stixrude, 2009; Scipioni et al., 2017; Stixrude et al., 2020).

All of our results are based on a simulation cell with $N = 135$ ($3 \times 3 \times 3$ supercell). The cell shape is cubic corresponding to the symmetry of the stable crystalline perovskite structure at high temperature (Stixrude et al., 2007). All calculations are performed in the canonical ensemble (constant N, V, T) with the temperature controlled by the Nosé-Hoover thermostat (Hoover, 1985). We assume a time-step of 1 fs for all simulations. Simulations were run for at least 5 ps, with the last 4 ps used to collect thermodynamic averages and the velocity autocorrelation function. We confirmed that simulations of twice this duration produced results that did not differ significantly, including the pressure, the internal energy, and the entropy (Fig. S2). We also confirmed that these properties did not differ significantly in simulations with a greater system size (1080 atoms) (Fig. S2). Uncertainties in time-averaged properties are computed with the blocking method (Flyvbjerg and Petersen, 1989). For the liquid, at each volume we first produce a melt at 10,000 K, and then cool isochorically to the temperatures of interest. For the solid, all simulations are initiated with the cubic perovskite structure and we confirm that this structure is maintained throughout the course of the solid simulations.

We compute the velocities and the moments of the vibrational density of states as time derivatives of the trajectories of the atomic positions via polynomial interpolation (Press et al., 1992). We found that it was possible to reliably compute time derivatives of the velocity at least up to second order, sufficient to compute the second and fourth moments of the vibrational density of states from Eq. (16). In order to avoid noise and spurious periodic sound waves, which arise artificially from the boundary conditions (Haile, 1992), we damp the velocity auto-correlation function using a Gaussian such that the amplitude is reduced to 0.1 at 500 fs before taking the cosine transform. We ensure that the zero frequency limit of the vibrational density of states matches the self-diffusion coefficient as computed independently from the Einstein formula for the mean-squared displacement (Allen and Tildesley, 1989).

We compute the melting temperature as follows. We first compute the Helmholtz free energy of liquid and solid phases

$$F(V,T) = E(V,T) - TS(V,T) \tag{35}$$

where we obtain the internal energy E from the time average of our molecular dynamics simulations and S from the 2PT method. At each volume, we find the temperature T_m at which $\Delta F = F_L(V,T_m) - F_S(V,T_m) = 0$ via interpolation: we find the root of the quadratic fit to our values of ΔF at the three simulated temperatures (2000 K, 4000 K, 6000 K). Expanding the Gibbs free energy locally to second order in the volume difference yields the melting pressure (Desjarlais, 2013)

$$P_m(V,T) = \frac{P_L\sqrt{\beta_L} + P_S\sqrt{\beta_S}}{\sqrt{\beta_L} + \sqrt{\beta_S}} \tag{36}$$

where P_L and P_S are the pressures, and β_L and β_S are the compressibilities of the liquid and solid, respectively at $\Delta F = 0$. We obtain the compressibilities from Birch-Murnaghan third order finite strain equation of state fits to each isotherm of each phase from our molecular dynamics simulation results. The third order Birch-Murnaghan equation of state (Birch, 1978) has been widely used in theoretical and experimental studies of silicate liquids (Stixrude and Karki, 2005; de Koker and Stixrude, 2009; Thomas et al., 2012; Caracas et al., 2019) and we find that it provides an excellent fit to our results. The equations of state of the solid and liquid phases are shown in Fig. 3. A measure of the uncertainty in the determination of the melting pressure is by comparison with the first order approximation (Moriarty et al., 1984): $P_m(V,T) = (P_L + P_S)/2$, which differs from Eq. (36) by no more than 0.2 GPa.

In Eq. (12) and Eq. (27), the partial molar volumes of the atoms appear. We may compute the partial molar

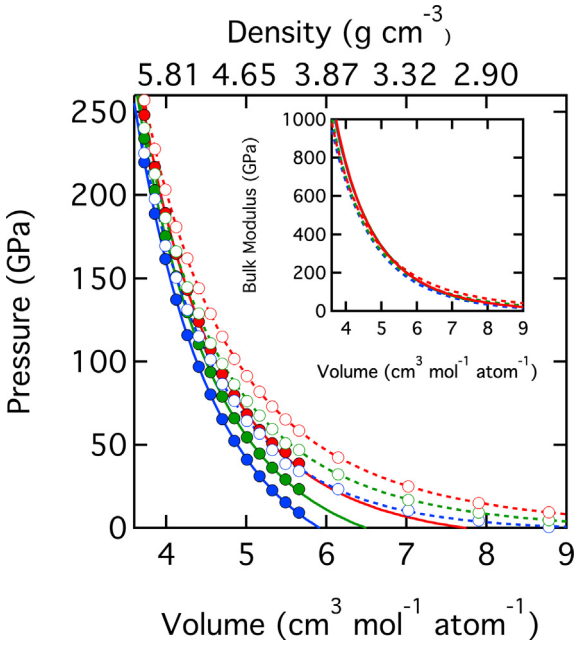

Fig. 3. Equation of state of liquid (dashed lines, open symbols) and solid (solid lines, filled symbols) at 2000 K (blue), 4000 K (green), and 6000 K (red). The inset shows the bulk modulus determined from the equation of state fits for liquid (dashed lines) and solid (solid lines) along the same isotherms. (For interpretation of the references to colour in this figure legend, the reader is referred to the web version of this article.)

volumes by performing simulations in which we vary the number of atoms of type α (French et al., 2016)

$$\bar{V}_\alpha = \frac{V}{K_T}\left(\frac{\partial P}{\partial N_\alpha}\right)_{V,T,N_\beta} = \frac{V}{K_T}\frac{P(V,T,N_\alpha+i_\alpha)-P(V,T,N_\alpha-j_\alpha)}{i_\alpha+j_\alpha} \tag{38}$$

where the first equality is exact and the second is exact in the limit $N \to \infty$. We check the internal consistency of these computations by comparing the bulk modulus computed from the changes in pressure

$$K = \sum_\alpha N_\alpha \left(\frac{\partial P}{\partial N_\alpha}\right)_{V,T,N_\beta} \tag{39}$$

to that from the equation of state fit described above (Fig. 3). At the smallest volume, we obtain robust results for the partial molar volumes and the bulk modulus with $i_\alpha = j_\alpha = 1$. At the largest volume, we use $i_\alpha = j_\alpha = 2$. We compare our results to a simplification of the 2PT method, in which the partial molar volumes are replaced by the so-called one-fluid approximation (Lai et al., 2012)

$$\bar{V}_\alpha = \frac{V}{N} \tag{40}$$

for all α, where V is the total volume and N is the number of atoms.

Our results (Table 1) show that the partial molar volume of the three atoms differ significantly. Nevertheless, despite the significant differences in partial molar volume, the entropy computed from the one-fluid approximation is nearly identical to that computed using the computed partial molar volumes: differences are less than 0.03 k/atom. Following previous work (Lai et al., 2012), we have therefore adopted the one-fluid approximation for all subsequent results shown in this study.

5. RESULTS

5.1. Entropy of the liquid

The entropy of the liquid computed from the 2PT method shows expected trends (Fig. 4): The entropy increases with increasing temperature and decreases on compression. The gas-like contribution and solid-like contribution to the entropy are similar in magnitude at the largest volume and 6000 K. While the solid-like contribution may increase or decrease on compression depending on temperature, the gas-like contribution decreases rapidly on compression, accounting for the decrease in the total entropy on compression. The solid like contribution to the entropy $k\sum_\alpha x_\alpha(1-f_\alpha)\int_0^\infty F_\alpha^s(v)W^s(v)dv$ may increase or decrease on compression because it is the product of

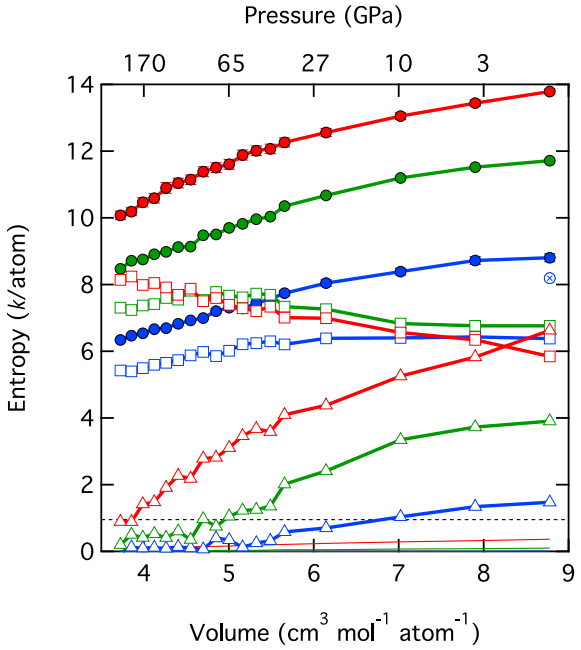

Fig. 4. The total entropy (filled circles), the solid-like $[k\sum_\alpha x_\alpha(1-f_\alpha)\int_0^\infty F_\alpha^s(v)W^s(v)dv$,open squares], gas-like $[k\sum_\alpha x_\alpha f_\alpha \int_0^\infty F_\alpha^g(v)W_\alpha^g dv$, open triangles], and electronic (thin solid lines) contributions to the total entropy at 2000 K (blue), 4000 K (green), and 6000 K (red), and the entropy of mixing (black dashed line). The crossed circle is the experimental value calculated at 2000 K from the fit equations provided in the experimental study (Richet et al., 1991). The top axis reports the pressure on the 2000 K isotherm. (For interpretation of the references to colour in this figure legend, the reader is referred to the web version of this article.)

two terms: the integral over the vibrational density of states, which uniformly decreases on compression, and the solid-like fraction $(1-f_\alpha)$, which uniformly increases on compression. The electronic entropy is everywhere less than 0.4 k/atom and diminishes on cooling and compression. The entropy of mixing for $CaSiO_3$: $-k\sum_\alpha x_\alpha \ln x_\alpha$ =0.96 k/atom.

We find agreement within uncertainty (Fig. 5) between the experimentally measured heat capacity and that calculated from our entropy results as follows

$$\bar{C}_V^{(S)}(\bar{T}) = \frac{S(T_2)-S(T_1)}{\ln(T_2/T_1)} \tag{41}$$

where the bar indicates the mean value of the heat capacity over the temperature interval interval $[T_1,T_2]$ with mean temperature temperature $\bar{T}$, the subscript V indicates the isochoric heat capacity and the superscript (S) specifies that

Table 1
Partial molar volumes (cm^3/mol/atom), the bulk modulus (GPa) computed from Eq. (39) and from the Birch-Murnaghan finite strain equation of state (K_{BM}, Fig. 3), and the entropy (k/atom) computed from the full theory (S_{full}) and from the one-fluid approximation ($S_{one\text{-}fluid}$) at 6000 K. Numbers in parentheses are the uncertainty in the last digits reported.

V	$\bar{V}_{Ca}$	$\bar{V}_{Si}$	$\bar{V}_O$	K	K_{BM}	S_{full}	$S_{one-fluid}$
3.7250	5.22 (40)	3.93 (39)	3.16 (42)	875 (55)	873	10.074 (130)	10.073 (130)
8.7780	16.6 (29)	9.6 (17)	5.9 (16)	42.9 (51)	45.5	13.756 (81)	13.784 (81)

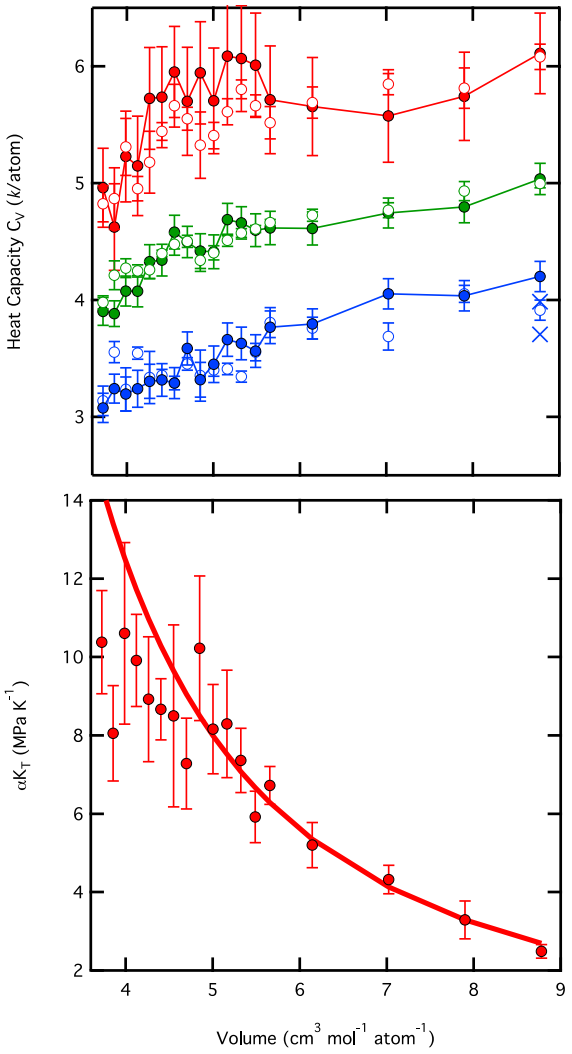

Fig. 5. (top) Heat capacity computed from the entropy (solid symbols) and from the internal energy (open symbols) via finite difference over the ranges: [2000 K,4000 K] (blue), [2000 K, 6000 K] (green) and [4000 K, 6000 K] (red). The latter two results are shifted upwards by 0.5 and 1.0 units respectively for clarity. The crosses show experimental values (Stebbins et al., 1984; Richet et al., 1991), where the latter has been corrected to the isochoric heat capacity using values of thermal expansivity and isothermal bulk modulus from the literature (Lange and Carmichael, 1987; Rivers and Carmichael, 1987). (bottom) The thermal pressure coefficient computed as the derivative of S with respect to V on the 6000 K isotherm (line) and from fluctuations (symbols). (For interpretation of the references to colour in this figure legend, the reader is referred to the web version of this article.)

the heat capacity is computed from the entropy. We can also use the heat capacity to test the internal consistency of our results by comparing the heat capacity calculated from the entropy to that calculated from the internal energy, which is known independently in our simulations (Braithwaite and Stixrude, 2019)

$$\bar{C}_V^{(E)}(\bar{T}) = \frac{E(T_2)-E(T_1)}{T_2-T_1} \tag{42}$$

The heat capacity computed from the internal energy and from the entropy are in good agreement (Fig. 5).

We further test the internal consistency of our results (Fig. 5) by comparing the volume dependence of the entropy to the thermal pressure coefficient αK_T, where α is the thermal expansivity and K_T is the isothermal bulk modulus via the following relations

$$\left(\frac{\partial S}{\partial V}\right)_T = \alpha K_T = \frac{\langle EP\rangle - \langle E\rangle\langle P\rangle}{kT^2} + \frac{Nk}{V} \tag{43}$$

The first equality is a thermodynamic identity. The second equality relates the thermal pressure coefficient to fluctuations in the internal energy and pressure (Allen and Tildesley, 1989). We compute $(\partial S/\partial V)_T$ numerically by fitting our results of entropy versus volume at 6000 K to a second order polynomial in $V^{-2/3}$ (de Koker and Stixrude, 2009) and taking the derivative of the fitted polynomial. We compute the thermal pressure coefficient independently from the fluctuation formula from our simulations. The agreement between these two methods is good: some deviation at the smallest volumes may be due to the limitations of our polynomial fit near the edge of the fitted range.

To better understand the contributions to the entropy, we compare the excess entropy to the two-body approximation (Eq. (4)) (Fig. 6). The two-body approximation is excellent over most of the range studied and perfect on the 6000 K isotherm. Deviations appear on cooling at the largest volumes and become as large as 1 k/atom at 2000 K and $V = 8.78$ cm^3 mol^{-1} atom^{-1} (0.6 GPa). These deviations indicate that the two-body approximation is not adequate at low temperature and pressure and that three- and higher-body correlations are important contributors to the excess entropy under these conditions.

The entropy of the liquid is mostly vibrational (Fig. 7). We examine the vibrational and configurational contributions to the entropy as follows

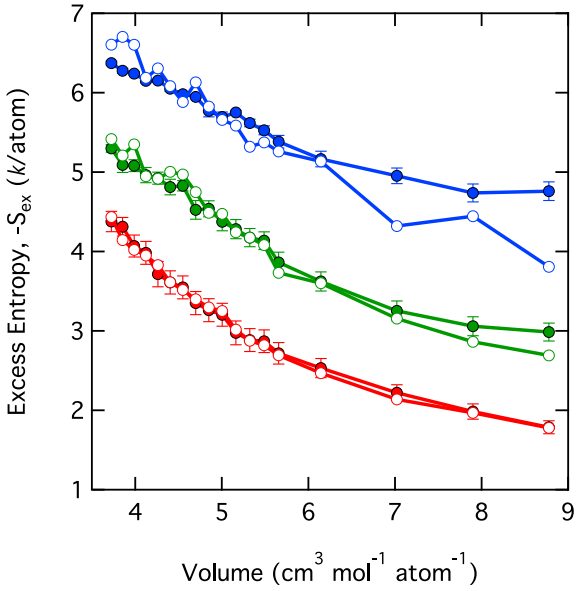

Fig. 6. Negative of the excess entropy (filled circles), compared with -s_2 (open circles) at 2000 K (blue), 4000 K (green), and 6000 K (red). (For interpretation of the references to colour in this figure legend, the reader is referred to the web version of this article.)

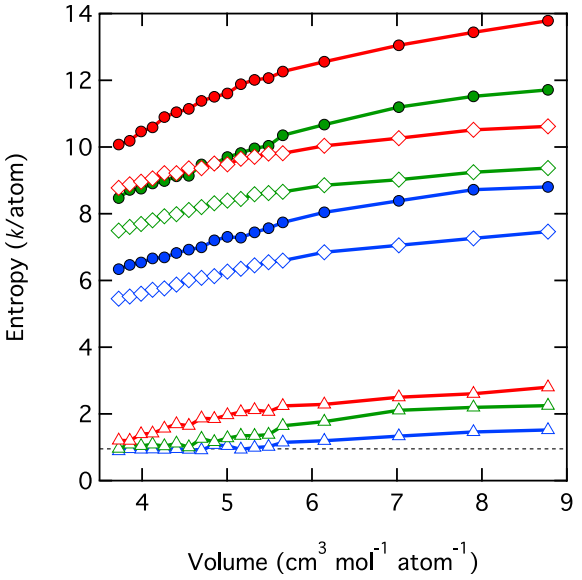

Fig. 7. The total entropy (filled circles), and the vibrational (open diamonds) and configurational (open triangles) contributions at 2000 K (blue), 4000 K (green), and 6000 K (red). The black dashed line is the entropy of mixing. (For interpretation of the references to colour in this figure legend, the reader is referred to the web version of this article.)

$$S_{vib}(V,T) = k\sum\nolimits_{\alpha} x_{\alpha} \int_0^{\infty} dv \left[F_{\alpha}^{s}(v) W^{s}(v)\right] \tag{44}$$

$$S_{conf}(V,T) = k\sum\nolimits_{\alpha} x_{\alpha} \int_0^{\infty} dv \left[f_{\alpha} F_{\alpha}^{g}(v) W_{\alpha}^{g} - f_{\alpha} F_{\alpha}^{s}(v) W^{s}(v)\right] - x_{\alpha} \ln x_{\alpha} \tag{45}$$

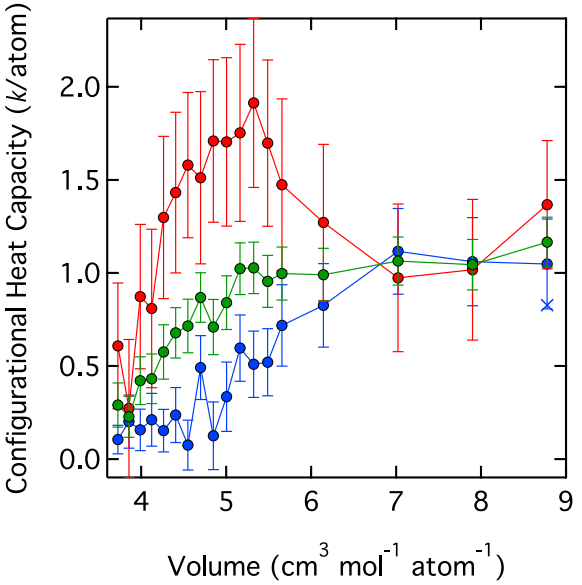

Fig. 8. The configurational heat capacity computed by finite difference of the configurational entropy over the ranges: [2000 K,4000 K] (blue), [2000 K, 6000 K] (green) and [4000 K, 6000 K] (red), compared with the experimental value (blue cross) (Richet et al., 1991). (For interpretation of the references to colour in this figure legend, the reader is referred to the web version of this article.)

The vibrational entropy makes up at least 75% of the total entropy over the range investigated. The proportion of the total entropy that is vibrational increases on cooling and compression, so that at 2000 K and the smallest volume, the entropy is 86% vibrational. The configurational contribution decreases on cooling and compression and reduces to the ideal mixing value (0.96 k/atom) at the smallest volumes at 2000 K and 4000 K.

The configurational heat capacity (Fig. 8) is 1 k/atom or nearly 25% of the total heat capacity at the largest volumes explored. It is nearly independent of volume and temperature (within uncertainty) from 6–9 cm^3 mol^{-1} $atom^{-1}$ (0.6–42 GPa). At smaller volumes, the configurational heat capacity decreases on compression, except over the range [4000 K, 6000 K] where it first increases on compression, reaching a peak value of nearly 2 k/atom at 5.32 cm^3 mol^{-1} $atom^{-1}$ (73 GPa), before decreasing on further compression. Our value of the configurational heat capacity agrees with the experimental value within uncertainty (Richet et al., 1991).

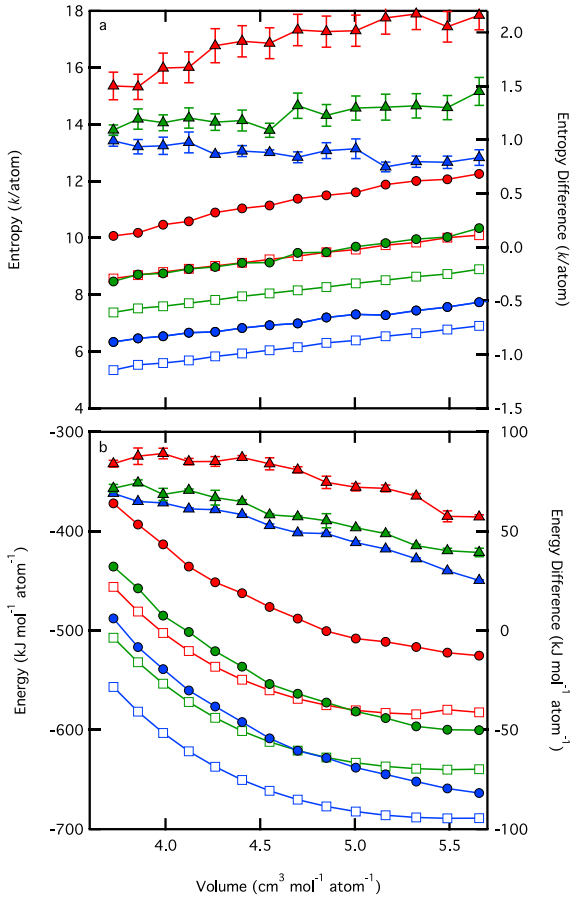

Fig. 9. a) Entropy (left-hand axis) and entropy difference (right-hand axis) and b) internal energy (left-hand axis) and internal energy difference (right-hand axis) of the liquid (filled circles) and perovskite (open squares), and the difference between the two phases (filled triangles, right-hand axes) at 2000 K (blue), 4000 K (green), and 6000 K (red) over the volume range of our solid phase simulations. (For interpretation of the references to colour in this figure legend, the reader is referred to the web version of this article.)

5.2. Free energy and melting

The contributions to the Helmholtz free energy difference between solid and liquid (Fig. 9)

$$\Delta F(V,T) = \Delta E(V,T) - T\Delta S(V,T) \tag{46}$$

show that the liquid has uniformly higher internal energy and entropy over the range considered. The contrast in internal energy and in entropy increase with increasing temperature at all volumes, reflecting the greater heat capacity of the liquid as compared with the solid. The effect of temperature on the contrast in internal energy and entropy diminishes on compression as the heat capacity of the liquid decreases on compression (Fig. 5).

The greater entropy of the liquid means that, with increasing temperature, the free energy of the liquid decreases more rapidly than that of the solid; at sufficiently high temperature, the liquid becomes the phase with the lowest free energy. Indeed, the Helmholtz free energy difference between liquid and solid decreases with increasing temperature (Fig. 10).

The melting curve of $CaSiO_3$ perovskite computed with the 2PT method agrees well with previous theoretical results based on alternative and independent methods (Fig. 11), including Clausius-Clapeyron integration and the ZW method (Braithwaite and Stixrude, 2019). The entropy of melting computed from the 2PT method also agrees with that determined from Clausius-Clapyron integration and the ZW method (Fig. 11) (Braithwaite and Stixrude, 2019).

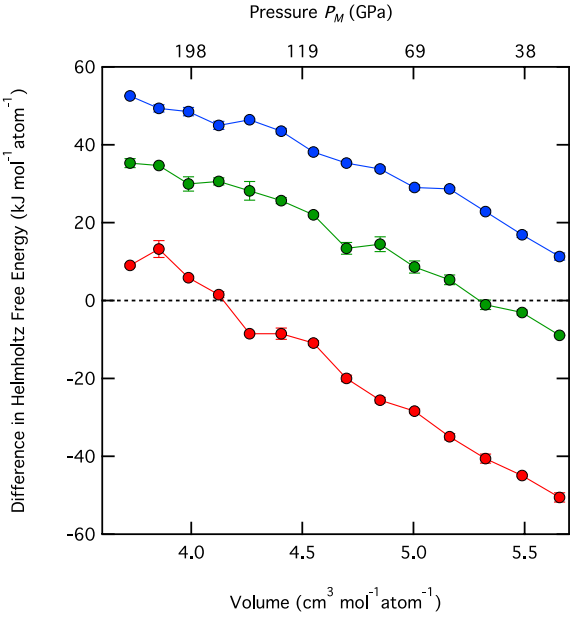

Fig. 10. Difference in free energy between the liquid and solid $\Delta F = F_L - F_S$ at 2000 K (blue), 4000 K (green), and 6000 K (red). The top axis reports the pressure on the melting curve (Eq. (36)). (For interpretation of the references to colour in this figure legend, the reader is referred to the web version of this article.)

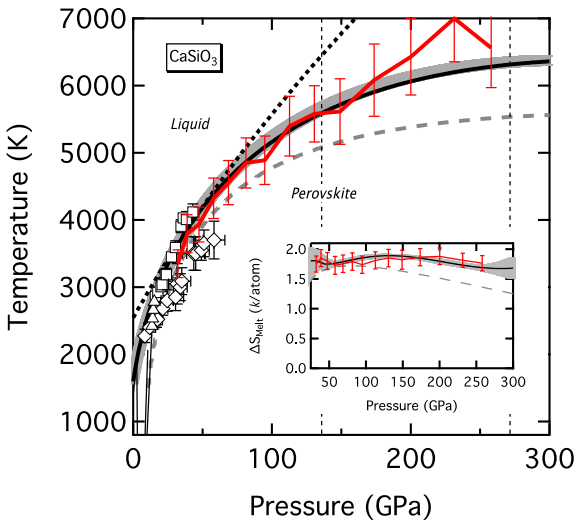

Fig. 11. Melting curve of $CaSiO_3$ perovskite computed with the 2PT method (red line and error bars) compared with the melting curve computed independently with the ZW method (black line) (Braithwaite and Stixrude, 2019) and via Claussius-Clapeyron integration (grey shading) (Braithwaite and Stixrude, 2019). Experimental measurements of melting are from (Gasparik et al., 1994) (triangles), (Shen and Lazor, 1995) (diamonds) and (Zerr et al., 1997) (squares). For comparison we show the $MgSiO_3$ melting curve (de Koker and Stixrude, 2009) (long gray dashed line), the Lindeman melting curve (bold short dashed line), and the solid–solid phase transformations from wollastonite to walstromite to larnite + $CaSi_2O_5$ titanite to perovskite (thin solid lines). The inset shows the entropy of melting ΔS_{Melt} (red with error bars) along the computed melting curve computed with the 2PT method (red line and error bars) compared with that determined independently by (Braithwaite and Stixrude, 2019) from Claussius-Clapeyron integration and the ZW method with interpolated enthalpy differences (black line with gray shading indicating uncertainties). For comparison we show as dashed lines the corresponding results for $MgSiO_3$ (de Koker et al., 2013).

5.3. Dynamics

We analyze further the vibrational and diffusional dynamics in the liquid and compare the former to the solid state. We characterize the vibrational dynamics via the zeroth moment of the vibrational density of states, which is the one most directly connected with the entropy

$$\theta_g = \frac{h}{k}\exp\left[\frac{\int_0^\infty \ln \nu F^s(\nu)d\nu}{\int_0^\infty F^s(\nu)d\nu}\right] \tag{47}$$

where the solid-like vibrational density of states $F^s = \sum_\alpha x_\alpha F^s_\alpha$, and the subscript g refers to the fact that the zeroth moment is also the geometric mean frequency (Barron et al., 1957). By multiplying with h/k, we work with the frequency in units of temperature to allow more direct comparison to the Debye temperature, which is central to the thermodynamic modeling of crystalline phases (Stixrude and Lithgow-Bertelloni, 2011). The results show that the vibrational density of states depends weakly on temperature and that it is primarily a function of volume in both liquid and solid phases (Fig. 12). The zeroth

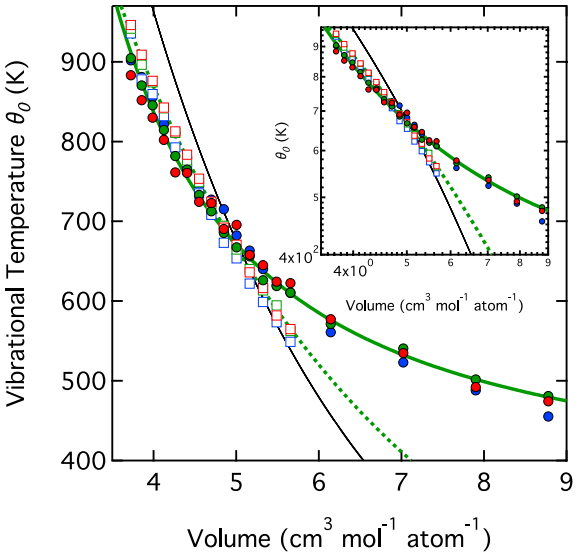

Fig. 12. Zeroth moment of the solid-like portion of the vibrational density of states of liquid (filled circles) and crystal (open squares) at 2000 K (blue), 4000 K (green), and 6000 K (red). Also shown are best fits to Eq. (48) of the 4000 K results for liquid (solid green line), and crystal (dashed green line). These best fits yield: θ_0=589 (2) K, γ_0=1.36(4), q=0.7(1) for crystal and θ_0 =623(2) K, γ_0=0.75 (1), q=-1.3(1) for liquid, with the reference volume $V_0 = 5.49$ cm^3 mol^{-1} atom^{-1} for both phases, i.e. the fictive volume of $CaSiO_3$ perovskite at ambient conditions (Shim et al., 2000). The black line is from HeFESTo (Stixrude and Lithgow-Bertelloni, 2011). The inset shows the same information but in log–log space. (For interpretation of the references to colour in this figure legend, the reader is referred to the web version of this article.)

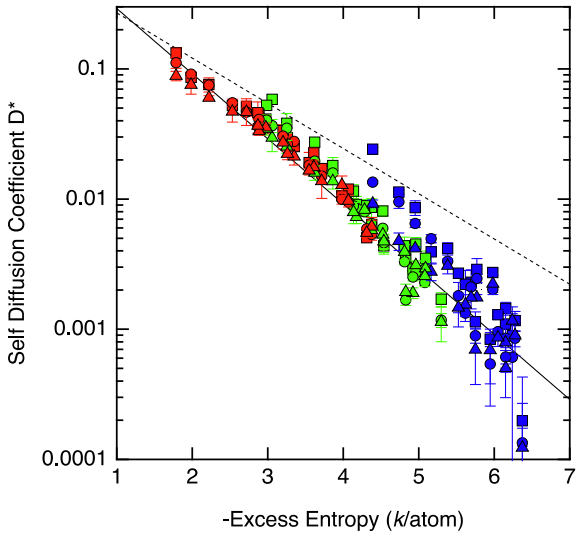

Fig. 13. Normalized self-diffusion coefficient (Eq. (49)), at 2000 K (blue), 4000 K (green), and 6000 K (red) of Ca (squares), Si (triangles) and O (circles). The solid line is a best fit to all the results: $D^* = 0.9\exp(1.2S_{ex})$, with the excess entropy S_{ex} in units of k/atom. The dashed line is from a fit to simulations of a number of different types of simple fluids: $D^* = 0.6\exp(0.8S_{ex})$ (Rosenfeld, 1999). (For interpretation of the references to colour in this figure legend, the reader is referred to the web version of this article.)

moment is similar in liquid and crystalline phases when compared at the same volume over most of the range explored. The vibrational frequency is systematically higher in the liquid as compared with the solid at large volume, and at small volume, the solid has the higher vibrational frequency. The volume dependence of the vibrational frequency in the two phases is therefore distinct.

To further characterize the volume dependence of the frequency, we fit the vibrational frequency of each phase to the expression

$$\theta_g = \theta_{g0}\exp\left\{\frac{\gamma_{g0}}{q}\left[1-\left(\frac{V}{V_0}\right)^q\right]\right\} \tag{48}$$

where $\gamma_g = -\left(d\ln\theta_g/d\ln V\right)_T$ is the vibrational Grüneisen parameter and $q = \left(d\ln\gamma_g/d\ln V\right)_T$. Whereas the solid phase results are best fit with a positive value of q, the liquid phase results require a negative value of q (Fig. 12). Therefore, the vibrational Grüneisen parameter of the liquid increases on compression while that of the solid decreases on compression.

Our results for the solid phase agree reasonably well with a thermodynamic model of mantle phases (Stixrude and Lithgow-Bertelloni, 2011). In this model, the vibrational density of states is represented by the Debye model for which the zeroth moment $\theta_g = \theta_D e^{-1/3}$ where θ_D is the Debye temperature. The thermodynamic model and our simulations agree well at the lower pressure (larger volume) extreme of our simulations on the solid phase. This is where the Debye temperature in the thermodynamic model is best constrained by experimental phase equilibria data. At higher pressures the thermodynamic model and our simulations diverge, which indicates that some improvement to the thermodynamic model should be investigated, either to the Grüneisen parameter or q.

We use our results to explore the notion of a corresponding states principle for liquid state dynamics (Fig. 13). A number of authors have shown that, for at least some classes of fluids, the self-diffusion coefficient and the viscosity are universal functions of the excess entropy when they are suitably non-dimensionalized using macroscopic thermodynamic properties (Rosenfeld, 1999)

$$D^*_\alpha = D_\alpha\frac{(N/V)^{1/3}}{(k_BT/m_\alpha)^{1/2}} \tag{49}$$

Over the range of our simulations, D_α varies by more than three orders of magnitude. Our results show that the scaling

$$D^* = 0.9\exp(1.2S_{ex}) \tag{50}$$

with the excess entropy in units of k/atom is quasi-universal and accounts for the self-diffusion coefficient to within a factor of two at most conditions; the root mean-squared misfit is 0.2 $\log_{10}$ units, similar to the difference between the scaling shown by our system and that found for simple fluids, including hard spheres, soft-spheres, the one-component plasma, and the Lennard-Jones fluid (Rosenfeld, 1999). We note that in detail there appear to be systematic deviations: our lower temperature results appear to depend more strongly on S_{ex} than the higher temperature results. We have therefore examined an alternative

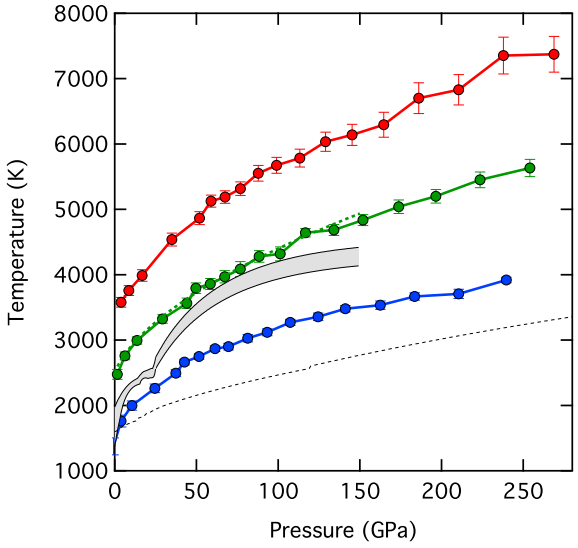

Fig. 14. Isentropes of $CaSiO_3$ liquid for entropies of 3.5 (3.9, blue), 4.0 (4.4, green), and 4.5 (5.0 red) kJ/kg/K, where the numbers in parentheses give the value of the entropy for a mean atomic mass of 21 g/mol. For comparison we also show the isentrope of $MgSiO_3$ liquid at 4.06 kJ/kg/K (green dashed line), the isentrope of the subsolidus mantle (black dashed line), and an estimate of the mantle melting interval (grey shading) (Stixrude et al., 2009). (For interpretation of the references to colour in this figure legend, the reader is referred to the web version of this article.)

scaling suggested by (Goel et al., 2011), in which $\ln D^*$ is a function of S_{ex}/T rather than S_{ex}. We find that this scaling is much inferior to the one presented in Fig. 13.

5.4. Liquid isentropes

We use our results of the absolute entropy as a function of volume and temperature to determine the isentropes of the liquid (Fig. 14). At each volume, we interpolate our results to find the temperature at which the absolute entropy matches the desired value and the pressure at that volume and temperature. The isentropic temperature increases with increasing pressure because the absolute entropy decreases on compression: at high pressure a larger temperature is required to achieve the same value of the entropy. The isentropic temperature increases very rapidly at low pressure and more gradually at high pressure. The isentropic gradient $(dT/dP)_S$ becomes steeper with increasing entropy. The geophysical significance of the computed isentropes is discussed below.

6. DISCUSSION

The 2PT method produces values of the absolute entropy of $CaSiO_3$ liquid that are in excellent agreement with independent determinations of the melting curve and the entropy of melting from Clausius-Clapeyron integration and the ZW method. The 2PT method has been found to yield accurate results for a wide variety of other types of fluids (Lin et al., 2003; Lai et al., 2012; Pascal and Goddard, 2012; Desjarlais, 2013; Wang et al., 2014). The method therefore shows promise as an efficient means of computing the entropy of silicate and oxide liquids relevant to geological processes. The method requires only the atomic trajectories and is therefore suited to any molecular dynamics simulation. Moreover, the trajectory is that of the system of interest: no auxiliary simulations are required, as would be in many alternative means of computing the free energy or the entropy, such as thermodynamic integration (Taniuchi and Tsuchiya, 2018), or particle insertion (Widom, 1963).

Our results for the absolute entropy provide important additional constraints on the fundamental thermodynamic relation of the liquid. The fundamental thermodynamic relation expresses the free energy in terms of its natural variables (e.g. $F(V,T)$) and specifies all thermodynamic properties of the system (Callen, 1960). Previous attempts to constrain the fundamental thermodynamic relation relied on simulated values of the pressure and the internal energy (de Koker and Stixrude, 2009). This approach leaves undefined an absolute entropy at the reference condition, which must be determined by comparing with experimental data. The present results provide the required value of the absolute entropy (Fig. 4) and permit a purely first principles determination of the fundamental thermodynamic relation.

Our results may also provide additional insight into the most suitable functional form of the fundamental thermodynamic relation. The entropy of the silicate liquid is dominated by the vibrational contribution, which makes up more than 75% of the entropy of the mantle regime (Fig. 7). An initial attempt to describe the fundamental thermodynamic relation of silicate liquids assumed that the entropy is entirely vibrational (Stixrude and Bukowinski, 1990). Our results show that this is clearly not correct, and that configurational contributions are important, especially at low pressure and high temperature. Nevertheless, the vibrational point of view may serve as a useful starting point for approximations. The vibrational point of view is distinct from that of Rosenfeld-Tarazona scaling (Rosenfeld and Tarazona, 1998) or other approaches that take the scaled hard-sphere fluid as a starting point (de Koker and Stixrude, 2009; Ghiorso et al., 2009; Jing and Karato, 2011).

The two-body approximation to the excess entropy (Eq. (4)) is excellent over most of the regime explored (Fig. 6). This result holds out the promise that the entropy of silicate liquids may be determined experimentally at high pressure. The x-ray structure factor has been measured for many silicate liquids at high pressure (Sanloup et al., 2013). The structure factor may be transformed to yield the radial distribution functions, from which the entropy (less any electronic contribution) may be computed from Eqs. (2)–(4). The two-body approximation is worst at low pressure and temperature where the entropy of many silicate liquids is already measured via calorimetry. The accuracy of the two-body approximation and the scaling of the self-diffusion coefficient (Eq. (50)) opens up the additional possibility of determining self-diffusion coefficients at high pressure from the experimental liquid structure, as also recently discussed by (Goel et al., 2011).

The two-body approximation, despite its simplicity of calculation, has not been widely used to estimate the

entropy of silicate liquids, although it was advocated by (Goel et al., 2011). One reason is that there have been few other calculations of the entropy of silicate liquids with which to evaluate the accuracy of this approximation. The good agreement that we find, over most of the volume-temperature range explored, between the two-body approximation and the 2PT method is therefore significant. The two-body approximation is well studied in the case of the hard sphere fluid. For the hard-sphere fluid, s_2 deviates significantly from the exact result (by as much as 0.4 k/atom at the highest density); the three-body term has been evaluated, and found to be significant (Baranyai and Evans, 1991). The fact that s_2 agrees as well as it does with the 2PT method in the case of $CaSiO_3$ liquid is therefore perhaps surprising. Clearly there are many differences between a hard sphere fluid and a silicate liquid, including the fact that the structure of silicate liquids is not close-packed and is strongly influence by charge ordering, the significance of which was recently emphasized (Scipioni et al., 2017). The situation therefore calls for careful study of the two-body approximation against experimental measurement and the 2PT method and other methods for the calculation of the entropy in a wide variety of silicate and oxide liquids.

One of the remarkable features of the thermodynamic properties of silicate liquids is the dependence of the Grüneisen parameter on compression. Whereas in almost all crystalline phases γ decreases on compression, in silicate liquids, γ increases on compression, corresponding to a negative value of q (Stixrude and Karki, 2005; Mosenfelder et al., 2007; Stixrude et al., 2009). The increase of γ with compression in silicate liquids has far reaching implications for our understanding of the initial thermal state of Earth, and the analysis of Hugoniot data (Stixrude et al., 2009).

Our results allow us to understand why the Grüneisen parameter increases on compression in silicate liquids. The increase originates in the vibrational contribution to the entropy, which dominates over most of the range studied, and which clearly shows the vibrational Grüneisen parameter increasing on compression (Fig. 12). Unlike crystals, the structure of the liquid changes on compression: the cation-oxygen coordination numbers increase. It is known that among crystalline polymorphs, the Grüneisen parameter increases with increasing coordination number, e.g. in metasilicates from pyroxene-, to garnet-, to perovskite-type structures. As the liquid structure changes on compression, the liquid adopts values of the Grüneisen parameter appropriate for the higher coordinated state.

The liquid state isentropes allow us to estimate the thermal state of a magma ocean following a giant impact (Fig. 14). The post-impact state may be isentropic, i.e. characterized by a uniform value of the entropy: dynamical simulations indicate an isentropic temperature profile is established in the magma ocean within 5–100 kyr after the giant impact, following a stably stratified regime caused by the greater entropy gain from the impact in the shallow mantle as compared with the deeper mantle (Nakajima and Stevenson, 2015). Simulations of the post-impact Earth have explored values ranging from 4-7 kJ/kg/K (Lock and Stewart, 2017). For an entropy of 4 kJ/kg/K, we find temperatures ranging from 3500 K at low pressure to 6000 K at the pressure of the Earth's core-mantle boundary (136 GPa). These values may somewhat overestimate the temperature of the bulk silicate Earth along the same isentrope because the mean atomic mass of $CaSiO_3$ exceeds that of the bulk silicate Earth. We estimate the magnitude of this effect by scaling the entropy by the mean atomic mass. In this approximation, the 4 kJ/kg/K isentrope of $CaSiO_3$ ($\bar{m} = 23.2$ g/mol) corresponds to the 4.4 kJ/kg/K isentrope of the bulk silicate Earth ($\bar{m} = 21$ g/mol). The efficacy of this approach is illustrated by comparing the isentropes of $CaSiO_3$ and $MgSiO_3$ liquid ($\bar{m} = 20.1$ g/mol): the 3.5 kJ/kg/K isentrope of $CaSiO_3$ is nearly identical to the 4.0 kJ/kg/K isentrope of $MgSiO_3$ (Fig. 14).

According to this analysis, 4.4 kJ/kg/K is the lowest entropy that is completely super-liquidus throughout the pressure regime of the mantle. The temperature at the core-mantle boundary along this isentrope (6000 K) therefore sets a lower bound to the temperature at the core-mantle boundary of a completely molten, isentropic Earth. The temperature at the core-mantle boundary post-giant impact may be considerably higher than 6000 K. For example, for a bulk silicate Earth entropy of 5 kJ/kg/K, the temperature at the core-mantle boundary is greater than 7000 K. We have not estimated the core-mantle boundary temperature along hotter isentropes because this would entail considerable extrapolation from our simulations. The temperature at the base of an isentropic magma ocean is an important reference because it may be the highest temperature at which extensive core-mantle chemical exchange occurred, and therefore may have influenced the initial composition of the core, for example, its initial complement of light impurities such as SiO_2 and MgO (Badro et al., 2018).

The isentropic temperature along the liquid state isentrope increases rapidly with increasing pressure. The slope is much greater than that of the average present-day mantle. Moreover, at high pressure the slope of the isentrope is steeper than that of the mantle liquidus. We have previously shown that the remarkable steepness of the liquid state isentrope arises from the increase of the Grüneisen parameter on compression (Stixrude et al., 2009). Here we confirm this result in a much more direct manner, by using the present determinations of the absolute entropy of the liquid.

7. CONCLUSIONS

The absolute entropy of silicate liquids has not been determined before by first principles methods, nor has it been measured experimentally at pressures greater than 1 bar, or temperatures greater than 2000 K. Our first principles predictions of the absolute entropy over the entire mantle pressure–temperature regime provide important insight into the behavior of silicate liquids and the connection between the entropy and other properties, such as liquid structure, vibrational and diffusional dynamics, and melting. The construction of the 2PT method demonstrates further connections, to foundational concepts from statistical mechanics, including the velocity autocorrelation function, and the vibrational density of states.

We have demonstrated that the 2PT method provides an attractive, internally consistent means of computing the absolute entropy. The calculation relies solely on the atomic trajectories: the velocity auto-correlation function, vibrational density of states, and all other ingredients of the 2PT method are computed only from knowledge of the atomic positions versus time. Moreover, the trajectory is that of the system of interest: no auxiliary simulations are required, as would be in many alternative means of computing the free energy, such as thermodynamic integration, adiabatic switching, or particle insertion. These features of the 2PT method make it particularly attractive for generalization to more complex multi-component silicate liquids, and the computation of chemical potentials.

Declaration of Competing Interest

The authors declare that they have no known competing financial interests or personal relationships that could have appeared to influence the work reported in this paper.

ACKNOWLEDGEMENTS

This research is supported by the European Research Council under Advanced Grant 291432 MoltenEarth (FP7) and by the National Science Foundation (EAR-1853388). Calculations were carried out using the IRIDIS cluster partly owned by University College London, ARCHER of the UK national high-performance computing service, MARENOSTRUM at the Barcelona Supercomputing Center of the PRACE Consortium, and the Hoffman2 Shared Cluster provided by the UCLA Institute for Digital Research and Education.

RESEARCH DATA

Data is included in the Electronic Annex.

APPENDIX A. SUPPLEMENTARY MATERIAL

Supplementary data to this article can be found online at https://doi.org/10.1016/j.gca.2021.03.015.

REFERENCES

Adam G. and Gibbs J. H. (1965) On temperature dependence of cooperative relaxation properties in glass-forming liquids. *J. Chem. Phys.* **43**, 139–146.

Alder B. J., Gass D. M. and Wainwright T. E. (1970) Studies in molecular dynamics.8. Transport coefficients for a hard-sphere fluid. *J. Chem. Phys.* **53**, 3813–3826.

Alfè D. (2005) Melting curve of MgO from first-principles simulations. *Phys. Rev. Lett.* **94**(23), 235701.

Allen M. P., Tildesley D. J. and Banavar J. R. (1989) Computer simulation of liquids. *Clarendon Press, Oxford* **42**(3), 105–106.

Badro J., Aubert J., Hirose K., Nomura R., Blanchard I., Borensztajn S. and Siebert J. (2018) Magnesium partitioning between earth's mantle and core and its potential to drive an early exsolution geodynamo. *Geophys. Res. Lett.* **45**, 13240–13248.

Baranyai A. and Evans D. J. (1989) Direct entropy calculation from computer-simulation of liquids. *Phys. Rev. A* **40**(7), 3817–3822.

Baranyai A. and Evans D. J. (1991) On the entropy of the hard-sphere fluid. *Z. Naturfors. Sect. A-J. Phys. Sci.* **46**, 27–31.

Barron T. H. K., Berg W. T. and Morrison J. A. (1957) The thermal properties of alkali halide crystals. 2. Analysis of experimental results. *Proc. Royal Soc. London Ser. A-Math. Phys. Sci.* **242**, 478–492.

Berens P. H., Mackay D. H. J., White G. M. and Wilson K. R. (1983) Thermodynamics and quantum corrections from molecular-dynamics for liquid water. *J. Chem. Phys.* **79**(5), 2375–2389.

Berne B. J., Boon J. P. and Rice S. A. (1966) On calculation of autocorrelation functions of dynamical variables. *J. Chem. Phys.* **45**, 1086–1096.

Birch F. (1978) Finite strain isotherm and velocities for single-crystal and polycrystalline NaCl at high-pressure and 300-degree-K. *J. Geophys. Res.* **83**, 1257–1268.

Blundy J., Cashman K. and Humphreys M. (2006) Magma heating by decompression-driven crystallization beneath andesite volcanoes. *Nature* **443**(7107), 76–80.

Born M. and Huang K. (1954) *Dynamical Theory of Crystal Lattices*. Clarendon Press, Oxford.

Braithwaite J. and Stixrude L. (2019) Melting of $CaSiO_3$ perovskite at high pressure. *Geophys. Res. Lett.* **46**(4), 2037–2044.

Callen H. B. (1960) *Thermodynamics*. John Wiley and Sons, New York.

Caracas R., Hirose K., Nomura R. and Ballmer M. D. (2019) Melt-crystal density crossover in a deep magma ocean. *Earth Planet. Sci. Lett.* **516**, 202–211.

Carnahan N. F. and Starling K. E. (1970) Thermodynamic properties of a rigid-sphere fluid. *J. Chem. Phys.* **53**(2), 600–603.

de Koker N., Karki B. B. and Stixrude L. (2013) Thermodynamics of the MgO-SiO2 liquid system in Earth's lowermost mantle from first principles. *Earth Planet. Sci. Lett.* **361**, 58–63.

de Koker N. and Stixrude L. (2009) Self-consistent thermodynamic description of silicate liquids, with application to shock melting of MgO periclase and $MgSiO_3$ perovskite. *Geophys. J. Int.* **178**(1), 162–179.

de Koker N. P., Stixrude L. and Karki B. B. (2008) Thermodynamics, structure, dynamics, and freezing of Mg2SiO4 liquid at high pressure. *Geochim. Cosmochim. Acta* **72**(5), 1427–1441.

Desjarlais M. P. (2013) First-principles calculation of entropy for liquid metals. *Phys. Rev. E* **88**(6), 062145.

Dickey J. M. and Paskin A. (1969) Computer simulation of lattice dynamics of solids. *Phys. Rev.* **188**, 1407–1418.

Douglass D. C. (1961) Self-diffusion and velocity correlation. *J. Chem. Phys.* **35**(1), 81–90.

Flyvbjerg H. and Petersen H. G. (1989) Error-estimates on averages of correlated data. *J. Chem. Phys.* **91**(1), 461–466.

French M., Desjarlais M. P. and Redmer R. (2016) Ab initio calculation of thermodynamic potentials and entropies for superionic water. *Phys. Rev. E* **93**(2), 022140.

Fultz B. (2010) Vibrational thermodynamics of materials. *Prog. Mater. Sci.* **55**, 247–352.

Gasparik T., Wolf K. and Smith C. M. (1994) Experimental-determination of phase-relations in the $CaSiO_3$ system from 8 to 15 GPa. *Am. Mineral.* **79**, 1219–1222.

Ghiorso M. S., Nevins D., Cutler I. and Spera F. J. (2009) Molecular dynamics studies of CaAl2Si2O8 liquid. Part II: Equation of state and a thermodynamic model. *Geochim. Cosmochim. Acta* **73**(22), 6937–6951.

Goel G., Lacks D. J. and Van Orman J. A. (2011) Transport coefficients in silicate melts from structural data via a structure-thermodynamics-dynamics relationship. *Phys. Rev. E* **84**(5), 051506.

Haile J. M. (1992) *Molecular Dynamics Simulation*. John Wiley and Sons, New York.

Hoover W. G. (1985) Canonical dynamics - equilibrium phase-space distributions. *Phys. Rev. A* **31**(3), 1695–1697.

Huber C., Bachmann O. and Manga M. (2009) Homogenization processes in silicic magma chambers by stirring and mushification (latent heat buffering). *Earth Planet. Sci. Lett.* **283**(1-4), 38–47.

Isbister D. J. and McQuarrie D. A. (1972) Calculation of coefficient of self-diffusion. *J. Chem. Phys.* **56**, 736–738.

Jing Z. and Karato S.-I. (2011) A new approach to the equation of state of silicate melts: An application of the theory of hard sphere mixtures. *Geochim. Cosmochim. Acta* **75**(22), 6780–6802.

Kresse G. and Furthmüller J. (1996) Efficiency of ab-initio total energy calculations for metals and semiconductors using a plane-wave basis set. *Comput. Mater. Sci.* **6**(1), 15–50.

Kresse G. and Joubert D. (1999) From ultrasoft pseudopotentials to the projector augmented-wave method. *Phys. Rev. B* **59**(3), 1758–1775.

Labrosse S., Hernlund J. W. and Coltice N. (2007) A crystallizing dense magma ocean at the base of the Earth's mantle. *Nature* **450**(7171), 866–869.

Lai P. K., Hsieh C. M. and Lin S. T. (2012) Rapid determination of entropy and free energy of mixtures from molecular dynamics simulations with the two-phase thermodynamic model. *Phys. Chem. Chem. Phys.* **14**, 15206–15213.

Lange R. A. and Carmichael I. S. E. (1987) Densities of Na_2O-K_2O-CaO-MgO-FeO-Fe_2O_3-Al_2O_3-TiO_2-SiO_2 liquids - new measurements and derived partial molar properties. *Geochim. Cosmochim. Acta* **51**(11), 2931–2946.

Lee S. K., Mosenfelder J. L., Park S. Y., Lee A. C. and Asimow P. D. (2020) Configurational entropy of basaltic melts in Earth's mantle. *PNAS* **117**(36), 21938–21944.

Lee S. K. and Stebbins J. F. (2002) Extent of intermixing among framework units in silicate glasses and melts. *Geochim. Cosmochim. Acta* **66**(2), 303–309.

Lin S.-T., Blanco M. and Goddard W. A. (2003) The two-phase model for calculating thermodynamic properties of liquids from molecular dynamics: Validation for the phase diagram of Lennard-Jones fluids. *J. Chem. Phys.* **119**(22), 11792–11805.

Lock S. J. and Stewart S. T. (2017) The structure of terrestrial bodies: Impact heating, corotation limits, and synestias. *J. Geophys. Res.-Planets* **122**(5), 950–982.

Mauro J. C., Yue Y., Ellison A. J., Gupta P. K. and Allan D. C. (2009) Viscosity of glass-forming liquids. *PNAS* **106**(47), 19780–19784.

McQuarrie D. A. (1976) *Statistical Mechanics*. Harper and Row, New York.

Meneses D. D., Malki M. and Echegut P. (2006) Optical and structural properties of calcium silicate glasses. *J. Non-Cryst. Solids* **352**(50-51), 5301–5308.

Mermin N. D. (1965) Thermal properties of the inhomogeneous electron gas. *Phys. Rev.* **137**(5A), A1441–A1443.

Moriarty J. A., Young D. A. and Ross M. (1984) Theoretical-study of the aluminum melting curve to very high-pressure. *Phys. Rev. B* **30**(2), 578–588.

Mosenfelder J. L., Asimow P. D. and Ahrens T. J. (2007) Thermodynamic properties of Mg_2SiO_4 liquid at ultra-high pressures from shock measurements to 200 GPa on forsterite and wadsleyite. *J. Geophys. Res.-Solid Earth* **112**, B06208.

Mysen B. O. and Richet P. (2018) *Silicate Glasses and Melts*, 2nd ed. Elsevier Science, Amsterdam.

Nakajima M. and Stevenson D. J. (2015) Melting and mixing states of the Earth's mantle after the Moon-forming impact. *Earth Planet. Sci. Lett.* **427**, 286–295.

Pascal T. A. and Goddard W. A. (2012) Hydrophobic segregation, phase transitions and the anomalous thermodynamics of water/methanol mixtures. *J. Phys. Chem. B* **116**(47), 13905–13912.

Perdew J. P., Ruzsinszky A., Csonka G. I., Vydrov O. A., Scuseria G. E., Constantin L. A., Zhou X. and Burke K. (2008) Restoring the density-gradient expansion for exchange in solids and surfaces. *Phys. Rev. Lett.* **100**(13), 136406.

Press W. H., Teukolsky S. A., Vetterling W. T. and Flannery B. P. (1992) *Numerical Recipes in FORTRAN: The Art of Scientific Comnputing*. Cambridge University Press, New York.

Retsinas A., Kalampounias A. G. and Papatheodorou G. N. (2016) Glass formation and Raman spectra of CaO-SiO_2 glasses towards the orthosilicate. *J. Phys. Chem. Solids* **99**, 19–24.

Richet P. (1984) Viscosity and configurational entropy of silicate melts. *Geochim. Cosmochim. Acta* **48**(3), 471–483.

Richet P. and Fiquet G. (1991) High-temperature heat capacity and premelting of minerals in the system MgO-CaO-Al_2O_3-SiO_2. *J. Geophys. Res.* **96**(B1), 445–456.

Richet P., Robie R. A. and Hemingway B. S. (1991) Thermodynamic properties of wollastonite, pseudowollastonite and $CaSiO_3$ glass and liquid. *Eur. J. Mineral.* **3**(3), 475–484.

Rivers M. L. and Carmichael I. S. E. (1987) Ultrasonic studies of silicate melts. *J. Geophys. Res.-Solid Earth and Planets* **92**(B9), 9247–9270.

Rosenfeld Y. (1999) A quasi-universal scaling law for atomic transport in simple fluids. *J. Phys.-Condensed Matter* **11**(28), 5415–5427.

Rosenfeld Yaako and Tarazona Pedr (1998) Density functional theory and the asymptotic high density expansion of the free energy of classical solids and fluids. *Mol. Phys.* **95**(2), 141–150.

Sanloup C., Drewitt J. W. E., Konôpková Z., Dalladay-Simpson P., Morton D. M., Rai N., van Westrenen W. and Morgenroth W. (2013) Structural change in molten basalt at deep mantle conditions. *Nature* **503**(7474), 104–107.

Scipioni R., Stixrude L. and Desjarlais M. P. (2017) Electrical conductivity of SiO2 at extreme conditions and planetary dynamos. *PNAS* **114**(34), 9009–9013.

Sharma R., Agarwal M. and Chakravarty C. (2008) Estimating the entropy of liquids from atom-atom radial distribution functions: silica, beryllium fluoride and water. *Mol. Phys.* **106**(15), 1925–1938.

Shen G. and Lazor P. (1995) Measurement of melting temperatures of some minerals under lower mantle pressures. *J. Geophys. Res.-Solid Earth* **100**(B9), 17699–17713.

Shim S.-H., Duffy T. S. and Shen G. (2000) The stability and P-V-T equation of state of CaSiO3 perovskite in the Earth's lower mantle. *J. Geophys. Res.-Solid Earth* **105**(B11), 25955–25968.

Stebbins J. F., Carmichael I. S. E. and Moret L. K. (1984) Heat-capacities and entropies of silicate liquids and glasses. *Contrib. Miner. Petrol.* **86**(2), 131–148.

Stishov S. M., Makarenko I. N., Ivanov V. A. and Nikolaenko A. M. (1973) Entropy of melting. *Phys. Lett. A* **45**, 18.

Stixrude L. and Bukowinski M. S. T. (1990) Fundamental thermodynamic relations and silicate melting with implications for the constitution of D''. *J. Geophys. Res.* **95**(B12), 19311–19325.

Stixrude L., de Koker N., Sun N. i., Mookherjee M. and Karki B. B. (2009) Thermodynamics of silicate liquids in the deep Earth. *Earth Planet. Sci. Lett.* **278**(3-4), 226–232.

Stixrude L. and Karki B. (2005) Structure and freezing of $MgSiO_3$ liquid in Earth's lower mantle. *Science* **310**, 297–299.

Stixrude L. and Lithgow-Bertelloni C. (2005) Thermodynamics of mantle minerals – I. Physical properties.. *Geophys. J. Int.* **162**(2), 610–632.

Stixrude L. and Lithgow-Bertelloni C. (2011) Thermodynamics of mantle minerals - II. Phase equilibria.. *Geophys. J. Int.* **184**(3), 1180–1213.

Stixrude L., Lithgow-Bertelloni C., Kiefer B. and Fumagalli P. (2007) Phase stability and shear softening in $CaSiO_3$ perovskite at high pressure. *Phys. Rev. B* **75** 024108.

Stixrude L., Scipioni R. and Desjarlais M. P. (2020) A silicate dynamo in the early Earth. *Nat. Commun.* **11**, 935–940.

Sun N., Stixrude L., de Koker N. and Karki B. B. (2011) First principles molecular dynamics simulations of diopside liquid at high pressure. *Geochmica et Cosmochimica Acta* **75**, 3792–3802.

Taniuchi T. and Tsuchiya T. (2018) The melting points of MgO up to 4 TPa predicted based on ab initio thermodynamic integration molecular dynamics. *J. Phys.-Condensed Matter* **30**(11), 114003.

Thomas C. W., Liu Q., Agee C. B., Asimow P. D. and Lange R. A. (2012) Multi-technique equation of state for Fe2SiO4 melt and the density of Fe-bearing silicate melts from 0 to 161 GPa. *J. Geophys. Res.-Solid Earth* **117**, 18.

Walker D., Agee C. B. and Zhang Y. X. (1988) Fusion curve slope and crystal liquid buoyancy. *J. Geophys. Res.-Solid Earth and Planets* **93**, 313–323.

Wallace D. C. (1972) *Thermodynamics of Crystals*, 1 ed. John Wiley and Sons, New York.

Wang J., Chakraborty B. and Eapen J. (2014) Absolute thermodynamic properties of molten salts using the two-phase thermodynamic (2PT) superpositioning method. *Phys. Chem. Chem. Phys.* **16**, 3062–3069.

Widom B. (1963) Some topics in theory of fluids. *J. Chem. Phys.* **39**, 2808–2812.

Zerr A., Serghiou G. and Boehler R. (1997) Melting of $CaSiO_3$ perovskite to 430 kbar and first in-situ measurements of lower mantle eutectic temperatures. *Geophys. Res. Lett.* **24**(8), 909–912.

Associate editor: Sung Keun Lee